



Efficient electrocatalytic reduction of CO₂ on Cu_xO decorated graphene oxides: an insight into the role of multivalent Cu in selectivity and durability

Wei Ni^a, Congxin Li^b, Xiaogang Zang^b, Min Xu^a, Silu Huo^a, Mingquan Liu^a, Zhiyu Yang^b, Yi-Ming Yan^{b,*}

^a School of Chemistry and Chemical Engineering, Beijing Institute of Technology, Beijing, 100081, People's Republic of China

^b State Key Lab of Organic-Inorganic Composites, Beijing Advanced Innovation Center for Soft Matter Science and Engineering, Beijing University of Chemical Technology, Beijing, 100029, People's Republic of China



ARTICLE INFO

Keywords:
carbon dioxide
copper oxides
multivalent Cu
formic acid
buffering effect

ABSTRACT

Copper oxides have been used as efficient electrocatalysts for electrocatalytic reduction of carbon dioxide (CO₂). However, understanding the catalytic mechanism of copper oxides electrocatalysts based on identifying their active species is difficult due to the presence of multivalent Cu, such as Cu(0), Cu(I) and Cu(II) species, during the reaction. Also, developing copper oxides electrocatalysts with high selectivity and long durability for carbon dioxide reduction reaction (CO₂RR) is highly desired. Herein, we report the preparation of Cu_xO decorated graphene oxides (G-Cu_xO-T) electrocatalyst by a controllable chemical reduction method. The G-Cu_xO-2 h electrocatalyst exhibits high selectivity towards HCOOH (81%) with a current density of 19.3 mA cm⁻² at -0.8 V vs RHE, as well as good durability (retaining 87.2% of initial activity after 9 hours continuous operation). Our study reveals that the observed high performance of G-Cu_xO-2 h electrocatalyst should not only benefit from the stabilized CO₂⁻ intermediate, but also contribute from the facilitated rate-limiting step of HCOO⁻ desorption, which are both closely related to an optimized Cu(I) content in the electrocatalyst. Moreover, a "buffering effect" is proposed to explain the promising durability of G-Cu_xO-2 h, where Cu(II) species should serve as sacrificial sources to supply Cu(I) from the thick subsurface layers, thereby balancing the content of Cu(I) at the surface and maintaining the activity of the electrocatalyst during the reaction. Our work provides crucial insights into the role of multivalent Cu in CO₂ reduction reaction, which are important for designing and preparing copper oxides based electrocatalysts with high selectivity and durability for electrochemical reduction of CO₂ into liquid fuels.

1. Introduction

The excessive utilization of fossil fuels leads to large amounts of CO₂ emissions and brings global energy and environmental crisis. To reduce the relying on nonrenewable fossil fuels, electrochemical CO₂ reduction has been widely investigated in the past few years. Electrochemical CO₂ reduction can achieve both objectives of reducing the carbon footprint and recycling the greenhouse gas back into fuels by utilizing renewable energy, such as solar, wind, or tidal power [1–4]. A number of electrocatalysts have been developed for electrochemical CO₂ reduction, including metal (for example, Au, Cu, Ag, Pd and Sn), metal oxides, and carbon-based materials [5]. Among these materials, copper oxides that serve as the most promising candidate can be able to selectively electrochemical reduction of CO₂ into formic acid (HCOOH), methane (CH₄), and ethanol (C₂H₅OH) [6]. However, the low faradic efficiency caused by competitive reduction of water itself to hydrogen is still a

major hurdle for further developing copper oxides based electrocatalysts for CO₂ reduction reactions (CO₂RR). In addition, for practical applications, the low selectivity for the conversion of CO₂ to a desired hydrocarbon remains a huge challenge [7]. Therefore, it is imperative to fabricate high performance copper oxides electrocatalysts which can simultaneously achieve high current density of CO₂RR and own high selectivity for products.

Recently, many efforts have been devoted to increase the activity of copper oxides electrocatalysts by controlling the surface morphology, designing the nanostructure, or tuning the compositional constitutions, which were realized by various strategies, such as reduction of thermally oxidized Cu or electrodeposited copper(I) oxide (Cu₂O) [8–10]. However, the related product distributions of CO₂RR obtained with those copper oxides electrocatalyst exhibits a large deviation among H₂, CO, HCOOH, CH₄, and C₂H₄. Several factors, such as electrocatalysts preparation methods, CO₂RR conditions, and grain boundary of

* Corresponding author.

E-mail address: bityanyiming@163.com (Y.-M. Yan).

nanoparticles, have been deemed as the main reasons responsible for the observed different results [11–13]. *In situ* and theoretical studies also revealed that multivalent copper states and oxygen moieties in the copper are contributed to adsorb the intermediate on the catalyst during CO₂RR, thus resulting in different products [14–17]. For instance, the residual Cu(I) phase was in favour of ethylene production on oxygen-plasma-treated Cu electrode [7]. Such large diversities in product selectivity stimulate us to further understand the origin of active species and identify the pathway of CO₂RR for copper oxides electrocatalysts. Moreover, durability is also important during CO₂RR, because the activity of CO₂RR in copper oxides electrocatalysts can be easily aggravated after long-term operation. Although several works have been performed to increase the durability of the CO₂RR electrocatalysts, more studies are still required to explain the deactivation phenomena of copper oxides electrocatalysts by considering the structural and compositional properties of the materials [18,19]. Therefore, it is of significant importance to better understand the selectivity and durability of the copper oxides, which is substantially meaningful for the design of selective and stable CO₂RR electrocatalysts.

Herein, we report the preparation of copper oxides (Cu_xO) decorated on graphene oxides (G-Cu_xO-T, T represents different reduction time in hydrogen) as high performance electrocatalysts for CO₂RR. By adjusting reduction time, the ratios of multivalent Cu ions in G-Cu_xO-T electrocatalyst can be concisely controlled in a facile manner. We found that the G-Cu_xO-2 h not only displayed the highest Faradaic efficiency (FE) of 81% for HCOOH production with a current density of 19.3 mA cm⁻² at -0.8 V vs. RHE, but also showed an excellent long-term durability with only 12.8% loss of initial activity after 9.0 hours potentiostatic test for CO₂RR. Interestingly, we observed the clear dependence of both FE of HCOOH and durability on the T (reduction time) value for the prepared G-Cu_xO-T electrocatalysts. Mechanistic study revealed that Cu(I) can dramatically stabilize the CO₂⁻ intermediate meanwhile weaken the binding strength for HCOO*, thus exposing more active site on the surfaces of electrocatalysts and enhancing the selectivity for HCOOH production at G-Cu_xO-2 h electrode. Furthermore, we proposed that a “buffering effect” between Cu(I) and Cu(II) might be responsible for the observed durability for G-Cu_xO-2 h. An optimized ratio of Cu(I)/Cu(II) enables the supply of Cu(I) from the inside layer of copper oxides, where Cu(II) serves as a sacrificial agent to electrochemically reduced to Cu(I), thus maintaining high activity for HCOOH production during the CO₂RR. These findings are very important information for future study on copper oxides electrocatalysts for CO₂RR.

2. Results and discussion

Fig. 1a shows the synthesis procedures for Cu_xO decorated graphene oxides composites by using a modified template method in a wet-chemical system. Firstly, Copper sulfate and GO are evenly mixed in the solution by stirring vigorously. Due to the GO existence of numerous single electrons of carbon atoms, the surface of GO is negatively charged with the effect of large conjugated π-π bonds [20]. Thus, the positively charged Cu(II) can adsorb on GO and surface owing to electrostatic attraction. The GO@CuO precursor composites were thermally treated in a tube furnace (650°C for 2.0 hours), and then the composites were reduced in H₂ atmosphere. G-Cu_xO-T samples were prepared by controlling the reduction time to tune the compositional constitutions. Fig. 1b shows that the scanning electron microscopy (SEM) image of G-Cu_xO-2 h, revealing a typical nanosheet-like morphology and porous structure, while Fig. S3 shows the Cu_xO-2 h appear aggregation to some extent after remove GO template. Energy-dispersive X-ray spectroscopy (EDS) images (Fig. 1c) reveal that C, O, and Cu elements are homogeneously distributed over the entire G-Cu_xO-2 h sample, suggesting a uniform Cu_xO decoration on graphene oxides. The mass content of Cu in the samples was determined by inductively coupled plasma atomic emission spectrometry (ICP-AES), as shown in

Table S1. We noted that there is no obvious difference of Cu content for all samples, indicating Cu element can be well maintained during reduction in H₂. The high-resolution TEM image (Fig. 1d) shows the lattice fringe spacings of 2.13 Å and 2.30 Å, corresponding to the (200) facet direction of Cu₂O and the (111) facet direction of CuO, respectively [6,21]. It suggests that the as-prepared G-Cu_xO-2 h mainly consisted of Cu₂O and CuO, which might be caused by the reduction treatment in H₂ atmosphere. To further compare the effect of reduction time on the morphology, Fig. S1 shows the SEM images of obtained G-Cu_xO-T samples. As seen, all the samples exhibited similar structure, indicating that the samples can inherit the morphology and structure of GO template even after the reduction treatment in H₂. We noted that G-Cu_xO-2.5 h sample exhibited some aggregated nanoparticles at the surface, which might be caused by formation of Cu(0) after excessive reduction of Cu(I).

The structure and composition of G-Cu_xO-T electrocatalysts were further investigated. We carried out a series of characterizations including XRD, Raman and XPS. As proved by X-ray diffraction (XRD) patterns (Fig. 2a), all the G-Cu_xO-T electrocatalysts exhibited similar characteristic peaks of Cu₂O (JCPDS #34-1354) and CuO (JCPDS #44-0706) [22]. Particularly, for G-Cu_xO-2 h, the highest peak at 35° strongly confirms that it was composed of highest content of Cu₂O among all the samples [22]. Interestingly, the diffraction peaks density of CuO and Cu₂O increased along with the increase of reduction time to 2.0 hours. In contrast, the corresponding peaks of CuO and Cu₂O for G-Cu_xO-2.5 h decreased, while a new peak at 43° and 50° appeared which are assigned to Cu (111), (200) characteristic peaks, respectively [23]. The result clearly indicates that Cu nanoparticles appeared in G-Cu_xO-2.5 h sample, which also consistent with observations with SEM, as shown in Fig. S1g. Fig. 2b shows the Raman spectra of G-Cu_xO-T, where the D (near 1340 cm⁻¹) and G (near 1590 cm⁻¹) peaks are the characteristic peaks of a carbon crystal, corresponding to sp³-carbons and sp²-carbons in the carbon matrix, respectively [24]. The degree of disorder in the carbon matrix and the quantity of defects are indicated with the ratio of the intensity of the D-band to that of the G-band (I_D/I_G). Table S1 presents the calculated values of the I_D/I_G for all the samples. As seen, the I_D/I_G values increase along with the increasing of reduction time, indicating an increase in the number of the disorder or defects in the G-Cu_xO-T [24]. Fig. 2c shows Cu 2p XPS spectra of G-Cu_xO-T electrocatalysts. The signals of Cu 2p region were clearly recorded, where the peaks at 932.7 and 934.8 eV are attributed to Cu(I) and Cu(II) species, respectively [6]. Moreover, the change in relative intensity of the Cu 2p peaks clearly indicates the change of the ratios of Cu(I)/Cu(II) in G-Cu_xO-T electrocatalysts. Again, we noted that the Cu(0) peak appears at 934.3 eV for G-Cu_xO-2.5 h nanosheet, corresponding with Fig. S1g. The appear of Cu (0) led to the bad performance in CO₂RR. The XPS results clearly confirm that the content of multivalent Cu, such as Cu(0), Cu(I), and Cu(II), has a close dependence on the H₂ reduction time. As shown in Fig. S2, the G-Cu_xO-2 h exhibited a maximum content of Cu(I) of 52.7% among all samples. As a consequence, for CO₂RR and some other reactions, the active site in the copper-based catalyst is the interfacial Cu(I) or the dispersed CuO_x (x = 0.2–0.5) species on the surface [25,26]. Noteworthy, although several strategies have been proposed to tune the Cu(I) in the published works, the H₂ reduction used in this work is simple and controllable. As the G-Cu_xO-2 h possesses the highest Cu(I) content among all the samples, it was expected to exhibit highest performance for CO₂RR, which will be investigated in the following sections.

To evaluate the performance of the G-Cu_xO-T for CO₂RR, they were loaded onto glassy carbon electrode to serve as working electrodes. We have been aware of the problem for CO₂RR that Pt may dissolve from the counter electrode when exposed to high potentials [27,28]. Fig. S6 shows the CVs of the G-Cu_xO-T modified electrodes measured in N₂- and CO₂-saturated 0.5 M KHCO₃ solution using a typical H-type electrolytic cell to construct the three-electrode system, which was separated by a cation-exchange membrane (Nafion 115 DuPont) to prevent

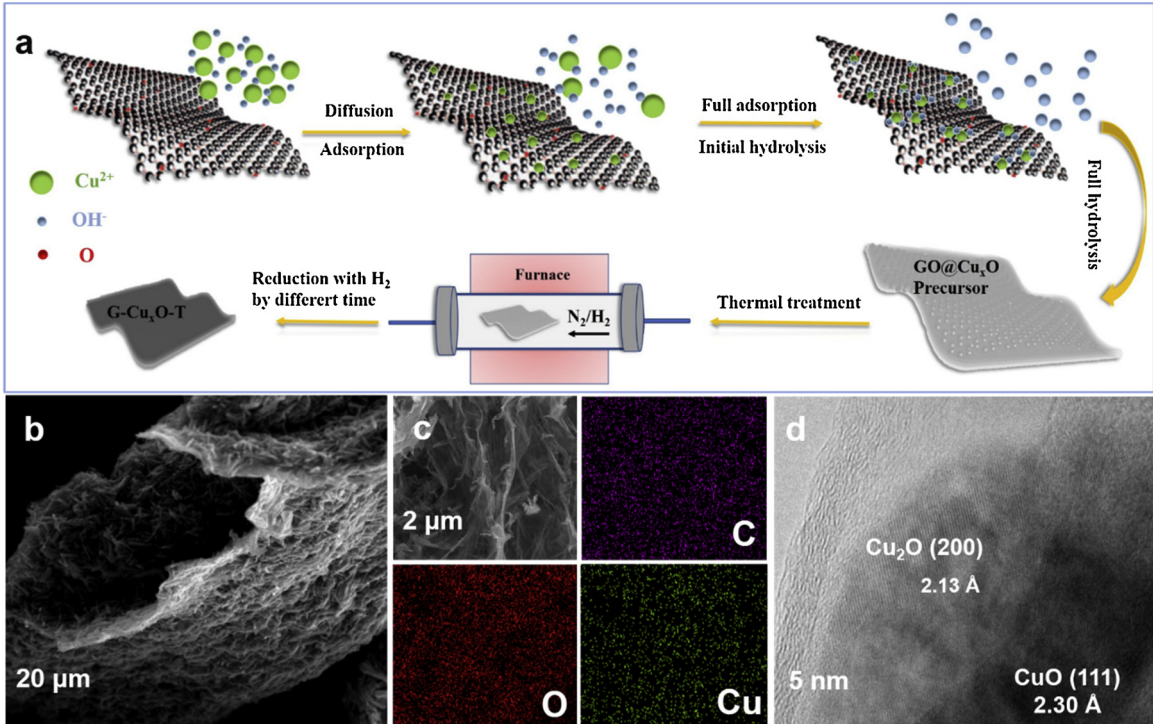


Fig. 1. (a) The strategy for synthesis of G-Cu_xO-T electrocatalysts. (b) Low magnification SEM image of the overall morphology of G-Cu_xO-2 h. (c) High magnification SEM image of the G-Cu_xO-2 h and EDS mapping analysis of C, O and Cu elements. (d) High-resolution TEM image of G-Cu_xO-2 h.

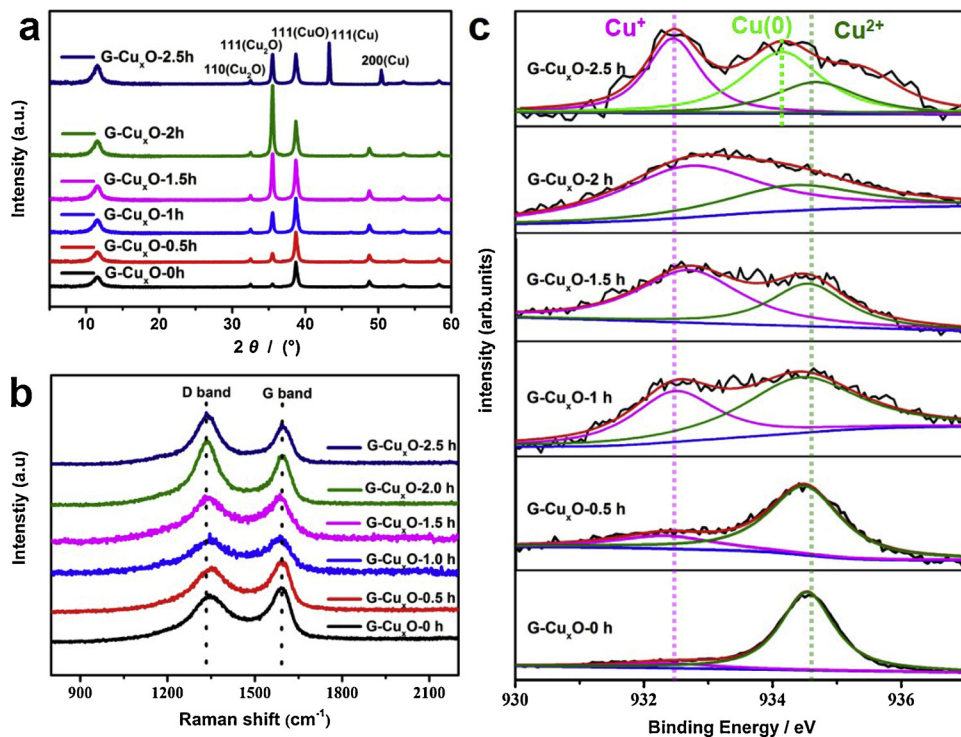
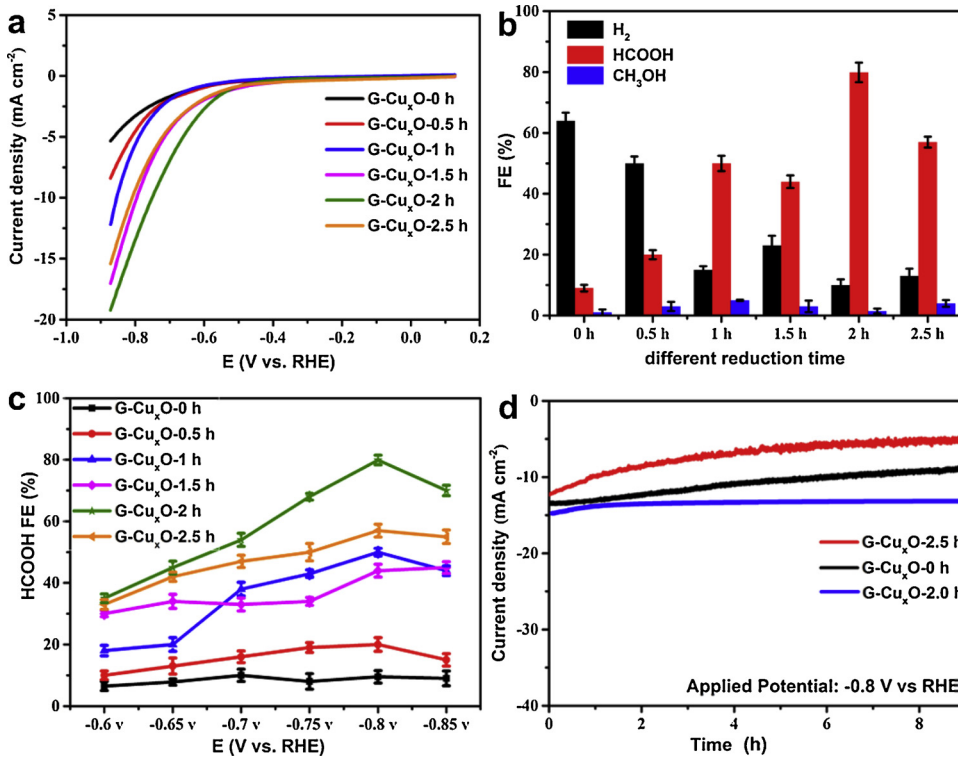


Fig. 2. (a) XRD patterns of G-Cu_xO-T samples. (b) Raman spectra of G-Cu_xO-T samples. (c) Cu 2p XPS spectra of G-Cu_xO-T samples. T represents different reduction time.

the mutual fouling in cathodic and anodic cells (see Fig. S5) [28–30]. As shown, a quite change was observed for the CVs of G-Cu_xO-T in N₂- and CO₂-saturated electrolytes. In the CO₂-saturated solution, the greatly increased current density at the potential lower than -0.45 V vs RHE should be attributed to the occurrence of the CO₂ electroreduction besides hydrogen evolution reaction (HER), which provides a direct

evidence for the reduction of CO₂ [31–33]. The as-prepared samples of linear sweep voltammetry (LSV) was recorded in the 0.5 M KHCO₃ electrolyte with a scan rate of 10 mV s⁻¹ in a potential range from 0.13 to -0.87 V vs. RHE so that to compare the overall catalytic activities. Once again, as shown in Fig. 3a, the G-Cu_xO-T electrocatalysts obviously exhibited dependence of CO₂RR activities on the reduction time



in H₂. Significantly, the G-Cu_xO-2 h electrocatalyst generated a current density of 19.3 mA cm⁻² at -0.8 V, which is the highest current density among all samples.

The products were identified by gas chromatography and ¹H nuclear magnetic resonance (¹H NMR) analysis. Formic acid (HCOOH), methanol (CH₃OH) and hydrogen (H₂) were detected with the as-prepared G-Cu_xO-T electrocatalysts. The molar quantity of HCOOH was measured by internal standard method of ¹H NMR (Supporting Information, Fig. S7). Fig. 3b shows the FE for each product at an applied potential of -0.8 V vs RHE. Each data point represents the average value of three independent measurements. The result of product analysis confirms that HCOOH, CH₃OH and H₂ were dominant products for all the G-Cu_xO-T electrocatalysts. Of note, among the main detected products at -0.8 V vs RHE, we are particularly focus on the selectivity of HCOOH on G-Cu_xO-T electrocatalysts. Previous study has shown that Cu/Cu₂O electrodes preferentially resulted in the production of HCOOH [23,34–37]. Thus, we further calculated the FE for HCOOH production on G-Cu_xO-T electrocatalysts at different applied overpotentials, as shown in Fig. 3c. Interestingly, the FE for HCOOH significantly increased along with the increasing of T value for G-Cu_xO-T samples at nearly all potentials. In particular, G-Cu_xO-2 h shows excellent selectivity for HCOOH with the highest FE of 81% among all the samples at -0.8 V vs RHE. In contrast, G-Cu_xO-2.5 h exhibited the lower FE of 56% for HCOOH production. Again, the results suggest that FE for HCOOH has a clear dependence on the reduction time, while 2.0 hours reduction results in highest FE value for HCOOH production. To clarify the origin of the FE, the performance of control samples, such as GO and Cu_xO-2 h, were also examined for CO₂RR and their FE values for HCOOH were recorded. As shown in Figs. S8 and S9, the small FE values for HCOOH of 6.8% and 29.7% were obtained for GO and Cu_xO-2 h at -0.8 V vs RHE, respectively. Notably, the selectivity and durability observed with the G-Cu_xO-2 h electrode are very competitive compared with that of copper-based electrocatalysts, as shown in Fig. S10 and Table S3. We assumed that the observed high FE for HCOOH at G-Cu_xO-2 h electrocatalyst should be attributed to a reasonable synergistic effect between Cu_xO and GO, as well as an optimized ratio of multivalent Cu tuned by the reduction time, rather than the morphology of the

Fig. 3. (a) Single reductive LSV results in CO₂-saturated 0.5 M KHCO₃ aqueous solution. (b) The FE of H₂, HCOOH and CH₃OH for G-Cu_xO-T electrocatalysts. E = -0.8 V vs RHE. (c) FE for HCOOH production at different applied potentials. (e) Plot of current density vs time for the G-Cu_xO-0 h, G-Cu_xO-2 h, and G-Cu_xO-2.5 h electrocatalysts at a constant potential of -0.8 V vs RHE.

samples. It has been reported that GO doping can favor the CO₂ adsorption and accelerated the electron charge transfer [38]. Also, an electronic interactions between GO and the supported Cu_xO might modify the electronic structure and enhance the activity of G-Cu_xO-T electrocatalysts [39–43]. For instance, by using in-situ infrared spectroelectrochemical method, Wang et al. found that graphene accelerated the electron charge transfer and further enhanced the adsorption of CO₂ for CO₂RR at Cu based electrocatalyst [44]. Thus, we further performed CO₂ adsorption isotherms measurements to elucidate CO₂ adsorption capacity in the presence of graphene oxide. As shown in Fig. S12, GO doping enhanced the CO₂ adsorption of G-Cu_xO-2 h nanosheets, which was the pre-requisite step for triggering further CO₂ reduction process.

Durability during long-term operation is another essential factor for assessing the performance of electrocatalysts for CO₂RR. Fig. 3d displays the recorded CO₂ reduction current performed at -0.8 V vs RHE for continuous 9.0 hours operation. As shown, G-Cu_xO-2 h only lost 13.8% of its initial current after 9.0 hours test, showing negligible decay during the operation. In comparison, G-Cu_xO-0 h and G-Cu_xO-2.5 h only retained 68.2% and 41.9% of their initial activity after the measurements, respectively. It's worth noting that the reduction of copper oxide to copper is favored at the negative potentials typically applied during CO₂ reduction. A controversial issue regarding oxide Cu catalysts is the oxidation state of the surface copper sites during the CO₂RR [14,45,46]. Cuenya et al. have demonstrated the existence of stable Cu⁺ species at highly negative potentials of ~-1.0 versus RHE during CO₂RR by using in-situ hard X-ray absorption spectroscopy (hXAS) [7]. Hwang et al. reported that the performance of Cu electrocatalyst with mixed copper states for CO₂ reduction. They found that the Cu based electrocatalyst maintained long-term stability during CO₂ electroreduction at a highly negative reduction potential, where the improved durability should be attributed to the existence of stable O-Cu bond in catalysts [47]. On the other hand, Zheng et al. found the Cu nanosheets can be well-protected from being oxidized by the adsorption of formate at the surface. They pointed out that formate should play an important role to keep atomic copper nanosheets ultrastable in the reduction of CO₂ [48]. In this work, we made ex-situ analysis of the oxidation states of the catalysts to

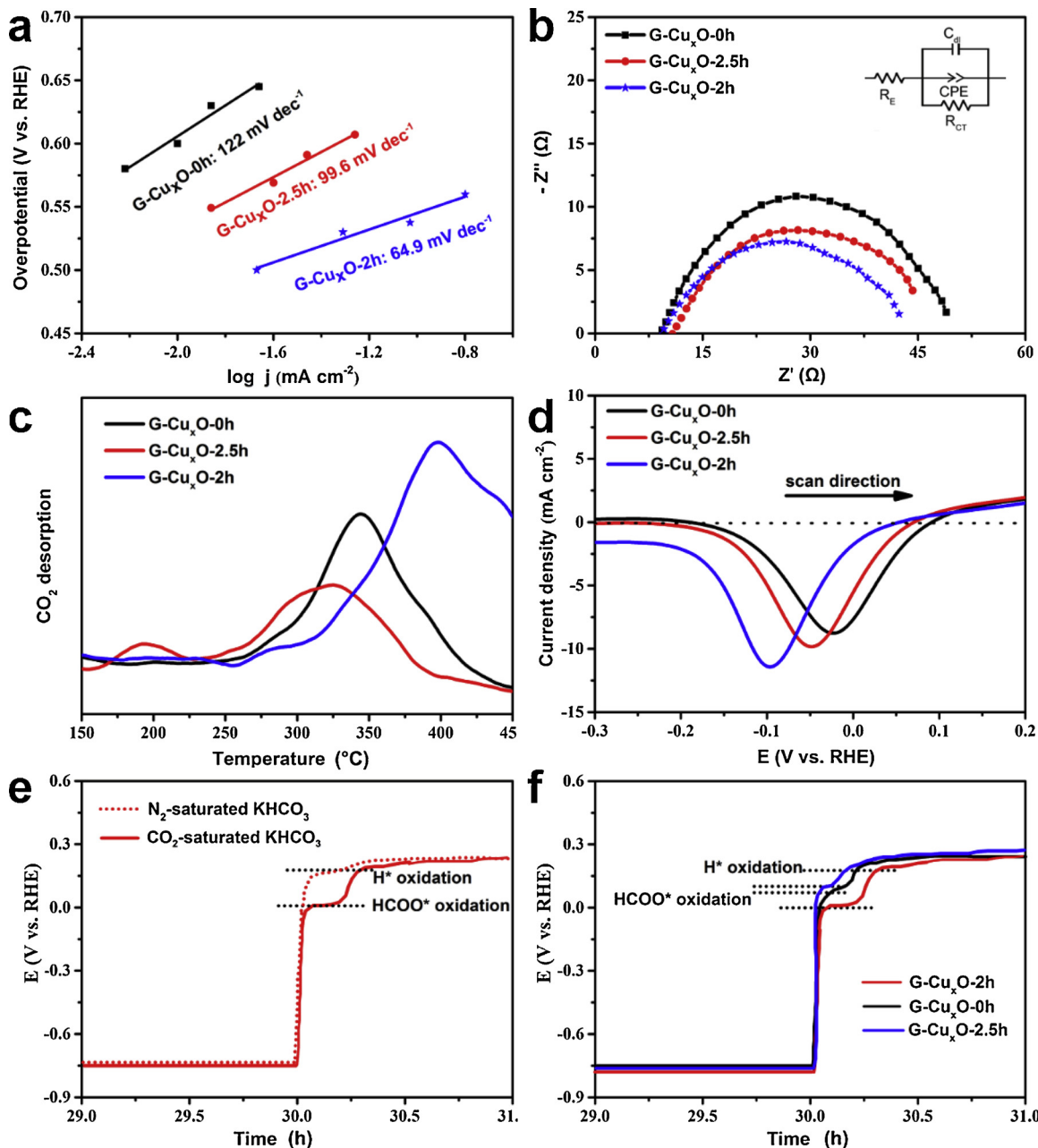


Fig. 4. (a) Tafel plots of the G-Cu_xO-0 h, G-Cu_xO-2 h, and G-Cu_xO-2.5 h electrocatalysts. (b) Nyquist plots of the three electrocatalysts in CO₂-saturated KHCO₃ electrolyte. (c) CO₂ TPD profiles of the G-Cu_xO-0 h, G-Cu_xO-2 h, and G-Cu_xO-2.5 h electrocatalysts at ramping rate of 5 K min⁻¹. (d) Single oxidative LSV scans at 50 mV s⁻¹ in N₂-saturated 0.1 M NaOH, illustrating surface adsorption of OH⁻ accompanying oxidation to electrocatalysts surface. (e) The galvanostatic step plots of oxidation potential of H* and HCOO* intermediates for G-Cu_xO-2 h in the absence and presence of CO₂-saturated KHCO₃ electrolyte. (f) The galvanostatic step plots of oxidation HCOO* intermediates for the three electrocatalysts in CO₂-saturated KHCO₃ electrolyte.

explore the role of multivalent Cu in the CO₂RR. To verify that a certain amount of HCOO⁻ might adsorb on the G-Cu_xO-2 h, temperature-programmed desorption/mass spectrometry (TPD-MS) measurements were performed to detect the species released from the nanosheets upon heating in vacuum. As shown in Fig. S13, a peak at a mass/charge ratio (m/z) of 45 confirms the presence of HCOO⁻ adsorbed at the surface of G-Cu_xO-2 h nanosheets. Thus, we assumed that our samples should be protected by the adsorbed HCOO⁻ from being oxidized during the being oxidized ex-situ analysis.

To explore the reasons for the observed variable performance of G-Cu_xO-T electrocatalysts, we further observe the insights into the relevant reaction kinetics during CO₂RR. As revealed in Fig. 4a, G-Cu_xO-0 h and G-Cu_xO-2.5 h samples exhibited Tafel slopes of 112 mV dec^{-1}

and 99.6 mV dec^{-1} , respectively. It indicates that the rate-determining step (RDS) for CO₂RR is the formation of CO₂⁻ (ads) species by the initial transfer of 1e⁻ from CO₂ (ads) [49–51]. In contrast, G-Cu_xO-2 h exhibited a low Tafel slope (64.9 mV dec^{-1}), which is close to the theoretical value of 59 mV dec^{-1} . It suggests that G-Cu_xO-2 h experienced a reduction mechanism encompassing a fast pre-equilibrium involving 1e⁻ transfer to form CO₂⁻ (ads) and RDS is the protonation of CO₂⁻ (ads) [2]. In other words, it appears that G-Cu_xO-2 h can facilitate CO₂ activation by effectively stabilizing the CO₂⁻ (ads) intermediate.

Fig. 4b shows the electrochemical impedance spectra (EIS) of the three electrocatalysts. Based on the EIS plot, the charge-transfer resistance (R_{ct}) of G-Cu_xO-2.5 h was calculated to be 32.0 Ω, which was lower than that of G-Cu_xO-2 h (34.0 Ω) and G-Cu_xO-0 h (39.6 Ω). The

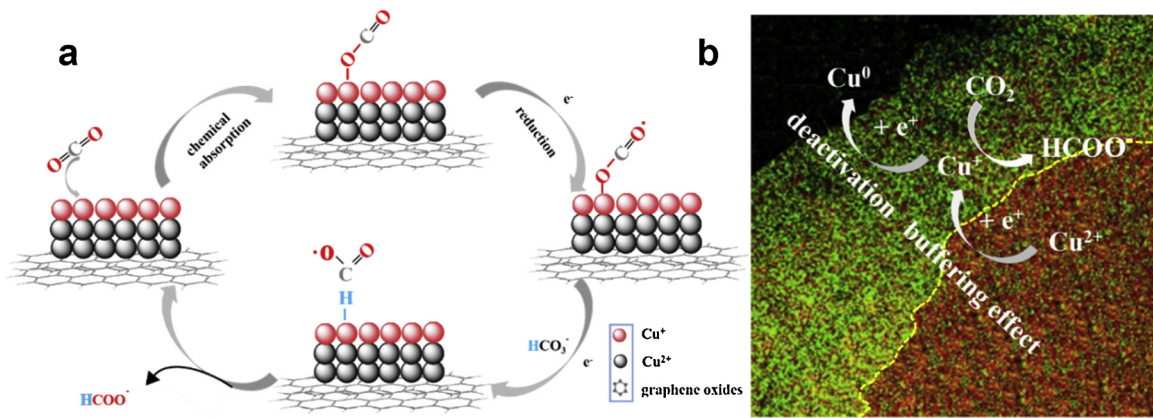


Fig. 5. (a) A proposed mechanism illustrating the steps of electrochemical CO_2 reduction and the formation of HCOOH occurring at the $\text{G-Cu}_x\text{O-2 h}$ electrocatalyst. (b) A proposed “buffering effect” illustrating the origin of durability of $\text{G-Cu}_x\text{O-T}$ electrocatalysts.

observed fast kinetic for $\text{G-Cu}_x\text{O-2 h}$ would facilitate the electron transport for the reaction, which is responsible for its high performance [52]. The high content of Cu(I) in $\text{G-Cu}_x\text{O-2 h}$ is believed to be responsible for this result which has been verified by Hemma Mistry et al. [7].

The dramatic differences in reaction kinetics inspire us to further observe the insights into the mechanism for CO_2 reduction at $\text{G-Cu}_x\text{O-T}$ electrocatalysts. To reveal the origin of the promoted CO_2 electro-reduction performances, electrochemical active surface area (ECSA) of the samples was performed. As shown in Fig. S11, three samples possessed nearly the same ECSA, where the double-layer capacitances (C_{dl}) of the samples are very similar, ranging from 8.25 to 5.06 m F cm^{-1} . In addition, the Table S3 also showed the Brunauer-Emmett-Teller (BET) specific surface area (SSA) of $\text{G-Cu}_x\text{O-0 h}$, $\text{G-Cu}_x\text{O-2 h}$, and $\text{G-Cu}_x\text{O-2.5 h}$ samples were $363 \text{ m}^2 \text{ g}^{-1}$, $346 \text{ m}^2 \text{ g}^{-1}$ and $337 \text{ m}^2 \text{ g}^{-1}$, respectively. The negligible difference in C_{dl} values and BET specific surface area indicates that the variation of ECSA and SSA of $\text{G-Cu}_x\text{O-T}$ electrocatalysts could be neglected. In other words, there are some other reasons responsible for the superior CO_2 reduction performance for $\text{G-Cu}_x\text{O-2 h}$ [53].

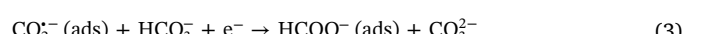
Next, we examined the CO_2 adsorption ability of the samples, which is an important factor influencing the whole CO_2 reduction performance. Fig. 4c shows the results of CO_2 temperature-programmed desorption (TPD) experiment measurements. As seen, comparing with $\text{G-Cu}_x\text{O-0 h}$ and $\text{G-Cu}_x\text{O-2.5 h}$, $\text{G-Cu}_x\text{O-2 h}$ reveals higher CO_2 adsorption signal indicates, indicating it owns higher binding energy for CO_2 adsorption. A recent study demonstrated that the promoted adsorption of CO_2 can facilitate CO_2 reduction [6,54]. Meanwhile, other theoretical and experimental works have been evident that Cu(I) is contributed to the strong CO_2 adsorption on the surface [6,17]. Correspondingly, the enhanced CO_2 adsorption enables stable coverage of various species on the catalyst surface and prolongs the residence time of the species, thereby offering more opportunities for the linkage formation of longer carbon chain species [6,55,56]. Taking these into account, we conclude that high content of Cu(I) at the surface of $\text{G-Cu}_x\text{O-2 h}$ should be responsible for its high activity and selectivity towards for CO_2RR .

In a typical process of electrochemical reduction of CO_2 to produce HCOOH , the adsorbed CO_2 is firstly transferred to CO_2^- (ads) as a reduced intermediate by accepting one electron from the electrode [52]. To further explore a possible role of CO_2^- during CO_2RR , we examined the adsorption ability of OH^- as a surrogate for CO_2^- [50]. We tested the binding affinity of CO_2^- for the three samples by using oxidative LSV scans in N_2 saturated 0.1 M NaOH electrolyte. Fig. 4d shows that the potential for surface OH^- adsorption on $\text{G-Cu}_x\text{O-2 h}$ electrocatalyst was -0.10 V , which is lower than that of $\text{G-Cu}_x\text{O-0 h}$ (-0.02 V) and $\text{G-Cu}_x\text{O-2.5 h}$ (-0.04 V), indicating that $\text{G-Cu}_x\text{O-2 h}$ electrocatalyst possessed stronger adsorption affinity of OH^- . In other words, $\text{G-Cu}_x\text{O-2 h}$ can

efficiently stabilize the CO_2^- intermediate and correspondingly facilitate HCOOH production [50].

Also, we tried to probe the selectivity of the $\text{G-Cu}_x\text{O-2 h}$ towards for HCOOH production by understanding the relation between intermediates and electrocatalysts during CO_2RR . We conducted the galvanostatic step to record the oxidation potential of H^* and HCOO^* intermediates by switching the applied current density switched from -9.7 mA cm^{-2} to $0.5 \mu\text{A cm}^{-2}$, during which the adsorbed intermediates were oxidized and the corresponding potential platforms were formed in the plots [51,57]. Fig. 4e shows the galvanostatic step experiments of $\text{G-Cu}_x\text{O-2 h}$ electrocatalyst in N_2 -saturated and CO_2 -saturated KHCO_3 electrolyte, respectively. Generally, in N_2 -saturated electrolyte, HER will dominate the reduction process. As seen, we can observe a characteristic potential platform at 0.18 V vs RHE that can be attributed to H^* oxidation. In comparison, after CO_2 was introduced into the electrolyte, a new platform emerged at 0.01 V vs RHE, corresponding to HCOO^* oxidation. The smaller oxidation potential of HCOO^* intermediate compare with H^* intermediate means the weaker binding strength of HCOO^* intermediate in $\text{G-Cu}_x\text{O-2 h}$ electrocatalyst. The two potentials platforms can be used as useful indicator of judging the competition reaction between HER and HCOOH production. Fig. 4f shows the galvanostatic step plots of $\text{G-Cu}_x\text{O-0 h}$, $\text{G-Cu}_x\text{O-2 h}$, and $\text{G-Cu}_x\text{O-2.5 h}$ electrocatalysts in CO_2 -saturated KHCO_3 electrolyte. The platforms of the three samples for H^* oxidation were located at the same potential, while the plateau potential for HCOO^* oxidation was 0.07 V for $\text{G-Cu}_x\text{O-0 h}$, and 0.1 V for $\text{G-Cu}_x\text{O-2.5 h}$, respectively. Again, $\text{G-Cu}_x\text{O-2 h}$ exhibited lowest potential for HCOO^* oxidation among these samples. Accordingly, it suggests that $\text{G-Cu}_x\text{O-2 h}$ possessed weakened binding strength for HCOO^* , which is beneficial for releasing HCOO^* intermediates and easily exposing the active site. As a consequence, $\text{G-Cu}_x\text{O-2 h}$ is more favorable for the production of HCOOH than other samples, which has been evident in Fig. 3b, c. Considering that three samples have similar structural and morphological properties, the observed apparent difference in HCOO^* oxidation should be ascribed to their compositional features.

Based on the above results and discussions, we proposed a reaction mechanism to understand the electrochemical reduction of CO_2 to HCOOH on $\text{G-Cu}_x\text{O-2 h}$, as shown in Fig. 5a. The elementary steps include:



It is suggested that CO₂ molecules initially adsorb on the surface of G-Cu_xO-2 h and hence undergo the following steps to produce formate. Subsequently, CO₂ (ads) molecule is reduced to the HCOO⁻ (ads) and the stabilized HCOO⁻ (ads) is then protonated and the formate product is finally generated. We noted that, for G-Cu_xO-2 h electrocatalyst, eq. 3 is most probably the RDS. This assumption is supported by the results in Fig. S14. By using KHCO₃/CO₂ as the buffer, the pH values slightly increased from 6.4 to 7.3 when the KHCO₃ concentrations were increased from 20 mM to 500 mM. As shown, the catalytic current densities for CO₂ reduction increase essentially linearly with the concentrations of HCO₃⁻, demonstrating the proton coupling process was the rate-determining step in CO₂ electroreduction. Combining with the Tafel slope of 64.9 mV dec⁻¹, which is close to 59 mV dec⁻¹, we presumably judge that the Eq. (3) is the rate-determining step (RDS). The kinetic analysis inferred the protonation of adsorption of CO₂⁻ (ads) to form HCO₃⁻ is the RDS [50–52]. In Eq. (3), proton transfer from HCO₃⁻ may activate a second electron transfer from the electrode, the concerted electron-proton reduction of adsorbed CO₂⁻ (ads) will lead to produce adsorbed formate product directly.

In addition to the selectivity, the oxidation state of Cu has a significant effect on durability during CO₂RR. Intensive efforts have been observed that Cu(I) will suffer deactivation during the electrochemical reduction of CO₂ [47,58,59]. Although it is experimentally difficult to unveil the mechanism behind the durability of Cu(I) species under the thermodynamically unfavourable conditions of CO₂RR, several possible mechanisms have been suggested to explain the phenomenon. For example, O₂ plasma treated surface causes strong oxygen binding, which is believed to benefit for the stabilization of copper oxides during the reaction [7,60]. Also, the high local pH is proposed to help to stabilize Cu(I) species by negatively shifting the overpotential for Cu₂O reduction [61,62]. Nonetheless, the role of multivalent Cu species in CO₂RR is still the subject of debate, and in situ tracking of the copper oxidation state with time resolution during CO₂RR is difficult. Very recently, a study on copper-based catalyst for methanol dehydrogenation discovered that a possible dynamic transformation between Cu(0) and Cu(I) species should be responsible for the stable performance of the catalyst [26]. Inspired by this work, we proposed a “buffering effect” mechanism to illustrate the durability of G-Cu_xO-2 h. TEM analysis (Fig. 1d) has been shown that the G-Cu_xO-2 h is composed of CuO and Cu₂O layers. To clearly present the mechanism, we simulated the distribution and marked the area of Cu(I) and Cu(II) in the TEM image, as shown in Fig. 5b. During the durability test, we found that the Cu(I) species were gradually reduced to Cu(0) species at the applied high overpotential (as shown in Figs. S15, 16), while the electrochemical CO₂RR performance decreased along with the consuming of Cu(I) species. However, for G-Cu_xO-2 h, the optimized ratio of Cu(I) / Cu(II) allows for a special balancing of Cu(I) content at the surface, where the CuO layer could serve as a sacrificial source to supply Cu(I) species by accepting electrons from electrode [7]. The constant Cu(I) concentration at the surface can maintain the activity of the electrocatalyst, thus achieving high durability. To verify this hypothesis, we further investigated the XPS of three electrocatalysts after durability test. Fig. S15 show that the Cu(I) content of G-Cu_xO-2 h was similar to its initial content, while the Cu(I) content of G-Cu_xO-2.5 h decreased after test for 9.0 hours. Interestingly, in spite that the Cu(I) content of G-Cu_xO-0 h surprisingly increased after the test, we did not observe the corresponding increasing of its activity. This might be caused by poor electrical contacting of the produced Cu(I) with the substrate, while more evidences are still needed to explain this observation. To further confirm that existence of dynamic transformation of multivalent Cu, Fig. S11 shows that SEM images of G-Cu_xO-T electrocatalysts after continuous 30 hours test. Clearly, Cu nanoparticles appear at the surface of all samples, indicating deactivation of electrocatalysts might due to the final production of Cu(0). Also, we noted that a high density of Cu nanoparticles observed at the surface of G-Cu_xO-2.5 h suggests it has a relative poor “buffering effect” during long-term test. Overall, we

deduced that an optimized ratio of Cu(I) / Cu(II) and a corresponding “buffering effect” between Cu(I) and Cu(II) might be responsible for the durability of the as-prepared electrocatalysts.

3. Conclusion

In conclusion, we have prepared Cu_xO decorated graphene oxides (G-Cu_xO-T) as efficient electrocatalyst for CO₂RR by a controllable chemical reduction method. This simple synthetic strategy can concisely control the content of Cu(0), Cu(I) and Cu(II), therefore allowing us to explore the role of multivalent Cu in selectivity and durability. An optimized G-Cu_xO-2 h sample exhibits higher intrinsic selectivity and durability for HCOOH production at lower overpotentials than the bulk Cu_xO-2 h and other G-Cu_xO-T samples. We demonstrated that the multivalent Cu should play crucial roles in determining the performance of G-Cu_xO-2 h. We found that Cu(I) contributes mainly to enhance adsorption of CO₂ and desorption of HCOO⁻, while Cu(II) helps to maintain the durability through a possible “buffering effect”. We noted that it is critical to use in-situ techniques to track the oxidation state of copper under CO₂ reduction conditions with time resolution for future studies. Nevertheless, this work highlights the importance of valence effect of copper oxides materials on their electrocatalytic activities and provides a strategy for designing efficient electrocatalysts for CO₂ electroreduction in the future.

Declaration of Competing Interest

The authors declare that they have no known competing financial interests or personal relationships that could have appeared to influence the work reported in this paper.

Acknowledgement

Financial support from the National Natural Science Foundation of China (grant nos. 21575016) and from the National Program for Support of Top-notch Young Professionals is gratefully acknowledged.

Appendix A. Supplementary data

Supplementary material related to this article can be found, in the online version, at doi:<https://doi.org/10.1016/j.apcatb.2019.118044>.

References

- [1] W. Zhu, R. Michalsky, Ö. Metin, H. Lv, S. Guo, C.J. Wright, X. Sun, A.A. Peterson, S. Sun, J. Am. Chem. Soc. 135 (2013) 16833–16836.
- [2] S. Gao, Y. Lin, X. Jiao, Y. Sun, Q. Luo, W. Zhang, D. Li, J. Yang, Y. Xie, Nature 529 (2016) 68–71.
- [3] C. Graves, S.D. Ebbesen, M. Mogensen, K.S. Lackner, Renewable Sustainable Energy Rev. 15 (2011) 11–23.
- [4] K.P. Kuhl, E.R. Cave, D.N. Abram, T.F. Jaramillo, Energy Environ. Sci. 5 (2012) 7050.
- [5] J. Qiao, Y. Liu, F. Hong, J. Zhang, Chem. Soc. Rev. 43 (2014) 631–675.
- [6] S. Lee, D. Kim, J. Lee, Angew. Chem. Int. Ed. Engl. 54 (2015) 14701–14705.
- [7] H. Mistry, A.S. Varela, C.S. Bonifacio, I. Zegkinoglou, I. Sinev, Y.W. Choi, K. Kisslinger, E.A. Stach, J.C. Yang, P. Strasser, B.R. Cuenya, Nat. Comm. 7 (2016) 12123.
- [8] A.S. Varela, W. Ju, T. Reier, P. Strasser, ACS Catal. 6 (2016) 2136–2144.
- [9] K.D. Yang, W.R. Ko, J.H. Lee, S.J. Kim, H. Lee, M.H. Lee, K.T. Nam, Angew. Chem. Int. Ed. Engl. 56 (2017) 796–800.
- [10] A. Dutta, M. Rahaman, N.C. Luedi, M. Mohos, P. Broekmann, ACS Catal. 6 (2016) 3804–3814.
- [11] X. Feng, K. Jiang, S. Fan, M.W. Kanan, J. Am. Chem. Soc. 137 (2015) 4606–4609.
- [12] X. Feng, K. Jiang, S. Fan, M.W. Kanan, ACS Cent. Sci. 2 (2016) 169–174.
- [13] D. Ren, Y. Deng, A.D. Handoko, C.S. Chen, S. Malkhandi, B.S. Yeo, ACS Catal. 5 (2015) 2814–2821.
- [14] A. Elert, F. Cavalca, F.S. Roberts, J. Osterwalder, C. Liu, M. Favaro, E.J. Crumlin, H. Ogasawara, D. Friebel, L.G. Pettersson, A. Nilsson, J. Phys. Chem. Lett. 8 (2017) 285–290.
- [15] M. Favaro, H. Xiao, T. Cheng, W.A. Goddard 3rd, J. Yano, E.J. Crumlin, Proc. Natl. Acad. Sci. U. S. A. 114 (2017) 6706–6711.
- [16] C. Liu, M.P. Lourenço, S. Hedström, F. Cavalca, O. Diaz-Morales, H.A. Duarte,

A. Nilsson, L.G.M. Pettersson, *J. Phys. Chem. C* 121 (2017) 25010–25017.

[17] P. De Luna, R. Quintero-Bermudez, C.-T. Dinh, M.B. Ross, O.S. Bushuyev, P. Todorović, T. Regier, S.O. Kelley, P. Yang, E.H. Sargent, *Nat. Catal.* 1 (2018) 103–110.

[18] Y. Hori, H. Konishi, T. Futamura, A. Murata, O. Koga, H. Sakurai, K. Oguma, *Electrochim. Acta* 50 (2005) 5354–5369.

[19] Z. Weng, X. Zhang, Y. Wu, S. Huo, J. Jiang, W. Liu, G. He, Y. Liang, H. Wang, *Angew. Chem. Int. Ed. Engl.* 56 (2017) 13135–13139.

[20] A.K.G.K.S. Novoselov, S.V. Morozov, D. Jiang, Y. Zhang, S.V. Dubonos, I.V. Grigorieva, A.A. Firsov, *Science* 306 (2004) 666–669.

[21] X.L. Deng, S. Hong, I. Hwang, J.S. Kim, J.H. Jeon, Y.C. Park, J. Lee, S.O. Kang, T. Kawai, B.H. Park, *Nanoscale* 4 (2012) 2029–2033.

[22] T.N. Huan, G. Rousse, S. Zanna, I.T. Lucas, X. Xu, N. Menguy, V. Mougel, M. Fontecave, *Angew. Chem. Int. Ed. Engl.* 56 (2017) 4792–4796.

[23] C.W. Li, M.W. Kanan, *J. Am. Chem. Soc.* 134 (2012) 7231–7234.

[24] X. Xu, H. Tang, M. Wang, Y. Liu, Y. Li, T. Lu, L. Pan, *J. Mater. Chem. A* 4 (2016) 16094–16100.

[25] B. Eren, C. Heine, H. Bluhm, G.A. Somorjai, M. Salmeron, *J. Am. Chem. Soc.* 137 (2015) 11186–11190.

[26] H. Yang, Y. Chen, X. Cui, G. Wang, Y. Cen, T. Deng, W. Yan, J. Gao, S. Zhu, U. Olsbye, J. Wang, W. Fan, *Angew. Chem. Int. Ed. Engl.* 57 (2018) 1836–1840.

[27] P.P. Lopes, D. Strmcnik, D. Tripkovic, J.G. Connell, V. Stamenkovic, N.M. Markovic, *ACS Catal.* 6 (2016) 2536–2544.

[28] J.G. Chen, C.W. Jones, S. Linic, V.R. Stamenkovic, *ACS Catal.* 7 (2017) 6392–6393.

[29] F.M. Le Zhang, Li Rong Zheng, Hai Feng Wang, Xiao Hua Yang, Hua Gui Yang, *ACS Catal.* 8 (2018) 11035–11041.

[30] H.S. Jeon, S. Kunze, F. Scholten, B. Roldan Cuanya, *ACS Catal.* (2017) 531–535.

[31] X. Guo, Y. Zhang, C. Deng, X. Li, Y. Xue, Y.M. Yan, K. Sun, *Chem. Commun.* 51 (2015) 1345–1348.

[32] R. Zhang, W. Lv, L. Lei, *Appl. Surf. Sci.* 356 (2015) 24–29.

[33] R.M.Y.J. Wu, M. Liu, P.P. Sharma, C.S. Tiwary, L. Ma, X. Zou, X. Zhou, B.I. Yakobson, J. Lou, P.M. Ajayan, *ACS Nano* 9 (2015) 5364–5371.

[34] S. Lee, S. Hong, J. Lee, *Catal. Today* 288 (2017) 11–17.

[35] E. Szaniawska, K. Bienkowski, I.A. Rutkowska, P.J. Kulesza, R. Solarska, *Catal. Today* 300 (2018) 145–151.

[36] T. Shinagawa, G.O. Larrazábal, A.J. Martín, F. Krumeich, J. Pérez-Ramírez, *ACS Catal.* 8 (2018) 837–844.

[37] H. Pan, S. Chowdhury, D. Premachandra, S. Olguin, M.D. Heagy, *ACS Sustain. Chem. Eng.* 6 (2017) 1872–1880.

[38] Z.-Y. Yang, L.-J. Jin, G.-Q. Lu, Q.-Q. Xiao, Y.-X. Zhang, L. Jing, X.-X. Zhang, Y.-M. Yan, K.-N. Sun, *Adv. Funct. Mater.* 24 (2014) 3917–3925.

[39] X. Li, G. Wang, L. Jing, W. Ni, H. Yan, C. Chen, Y.M. Yan, *Chem. Commun.* 52 (2016) 2533–2536.

[40] S. Oh, J.R. Gallagher, J.T. Miller, Y. Surendranath, *J. Am. Chem. Soc.* 138 (2016) 1820–1823.

[41] K. Tu, Q. Wang, A. Lu, L. Zhang, *J. Phys. Chem. C* 118 (2014) 7202–7210.

[42] C. Cheng, C. Zhang, X. Gao, Z. Zhuang, C. Du, W. Chen, *Anal. Chem.* 90 (2018) 1983–1991.

[43] S. Deng, V. Tjoa, H.M. Fan, H.R. Tan, D.C. Sayle, M. Olivo, S. Mhaisalkar, J. Wei, C.H. Sow, *J. Am. Chem. Soc.* 134 (2012) 4905–4917.

[44] J. Wang, L. Gan, Q. Zhang, V. Reddu, Y. Peng, Z. Liu, X. Xia, C. Wang, X. Wang, *Adv. Energy Mater.* 9 (2019).

[45] J.E. Pander, D. Ren, Y. Huang, N.W.X. Loo, S.H.L. Hong, B.S. Yeo, *ChemElectroChem* 5 (2018) 219–237.

[46] P. Grosse, D. Gao, F. Scholten, I. Sinev, H. Mistry, B. Roldan Cuanya, *Angew. Chem. Int. Ed. Engl.* 57 (2018) 6192–6197.

[47] S.Y. Lee, H. Jung, N.K. Kim, H.S. Oh, B.K. Min, Y.J. Hwang, *J. Am. Chem. Soc.* 140 (2018) 8681–8689.

[48] Q.Q. Dai, P. Wang, et al., *Sci. Adv.* 3 (2017) e1701069.

[49] M. Dunwell, Q. Lu, J.M. Heyes, J. Rosen, J.G. Chen, Y. Yan, F. Jiao, B. Xu, *J. Am. Chem. Soc.* 139 (2017) 3774–3783.

[50] S. Zhang, P. Kang, T.J. Meyer, *J. Am. Chem. Soc.* 136 (2014) 1734–1737.

[51] R. He, A. Zhang, Y. Ding, T. Kong, Q. Xiao, H. Li, Y. Liu, J. Zeng, *Adv. Mater.* 30 (2018) 1–7.

[52] S. Gao, Z. Sun, W. Liu, X. Jiao, X. Zu, Q. Hu, Y. Sun, T. Yao, W. Zhang, S. Wei, Y. Xie, *Nat. Comm.* 8 (2017) 14503.

[53] D. Ren, J. Fong, B.S. Yeo, *Nature communications* 9 (2018) 925.

[54] J. Xu, X. Li, W. Liu, Y. Sun, Z. Ju, T. Yao, C. Wang, H. Ju, J. Zhu, S. Wei, Y. Xie, *Angew. Chem. Int. Ed. Engl.* 56 (2017) 9121–9125.

[55] S. Sen, D. Liu, G.T.R. Palmore, *ACS Catal.* 4 (2014) 3091–3095.

[56] K.G. Schmitt, A.A. Gewirth, *J. Phys. Chem. C* 118 (2014) 17567–17576.

[57] A.H. C. H. Hamann, W. Vielstich, Wiley-VCH, Weinheim, Germany (1998).

[58] Y. Zhou, F. Che, M. Liu, C. Zou, Z. Liang, P. De Luna, H. Yuan, J. Li, Z. Wang, H. Xie, H. Li, P. Chen, E. Bladt, R. Quintero-Bermudez, T.K. Sham, S. Bals, J. Hofkens, D. Sinton, G. Chen, E.H. Sargent, *Nat. Chem.* 10 (2018) 974–980.

[59] H.J. Yang, H. Yang, Y.H. Hong, P.Y. Zhang, T. Wang, L.N. Chen, F.Y. Zhang, Q.H. Wu, N. Tian, Z.Y. Zhou, S.G. Sun, *ChemSusChem* 11 (2018) 881–887.

[60] D. Gao, I. Zegkinoglou, N.J. Divins, F. Scholten, I. Sinev, P. Grosse, B. Roldan Cuanya, *ACS Nano* 11 (2017) 4825–4831.

[61] A.S. Varela, M. Kroschel, T. Reier, P. Strasser, *Catal. Today* 260 (2016) 8–13.

[62] K.J.P. Schouten, E. Pérez Gallent, M.T.M. Koper, *J. Electroanal. Chem.* 716 (2014) 53–57.